



30

31

## Introduction

32

33

34

35

36

37

38

39

40

41

42

43

44

45

46

47

48

49

50

51

52

53

Titanium is one of the only crustal major elements capable of being incorporated to major-element concentrations in garnet whose substitution mechanisms and coordination remain poorly constrained. Exsolved rutile and ilmenite needles from ultra-high temperature and pressure (UHT and UHP, respectively) garnets suggest Ti solubility in garnet increases with increasing metamorphic grade. The presence of exsolved rutile and ilmenite in garnet has therefore been suggested as a possible indicator of high-grade metamorphism (Bishop et al. 1978; Snoeyenbos et al. 1995; Zhang et al. 2003; Tropper et al. 2005; Hwang et al. 2007; Ague and Eckert 2012; Proyer et al. 2013). In addition to the relevance for understanding high-grade metamorphism, Ti in garnet could be utilized to develop novel exchange or trace-element geothermobarometers. To assess the potential of Ti in garnet for understanding metamorphic processes, it is critical to understand the substitution (mechanisms and coordination) of Ti in garnets over a wide range of geologic environments.

If the Ti content of garnet is high enough, major-element chemical trends can be used to infer the substitution mechanisms for Ti in garnet. In synthetically-grown garnets, major element trends reveal that Ti incorporation at simulated eclogite- and granulite- facies conditions occurs primarily on the octahedral site via multiple substitution mechanisms (Ackerson et al., this issue). While this is a useful insight, there are significant limitations to the information obtainable from major-element correlations, primary among them being that Ti coordination is inferred rather than

54 directly measured. In addition, the conditions at which garnets can be grown  
55 synthetically in natural bulk compositions (>800 °C, >1.2 GPa) are generally more  
56 extreme than the crystallization environments of many crustal garnet-bearing  
57 metamorphic rocks. Most naturally-occurring garnets have Ti contents at or below  
58 the analytical uncertainty of the major elements measured using electron probe  
59 microanalysis (EPMA), making studies of substitution mechanisms and coordination  
60 via EPMA infeasible.

61 X-ray absorption fine structure (XAFS) spectroscopy can be utilized to  
62 directly determine the coordination and valence state of Ti in both synthetic and  
63 natural garnets at concentrations lower than the resolution of EPMA-based major-  
64 element chemical trends. Specifically, the energy and peak intensity of the Ti K-edge  
65 pre-edge feature is dependent on Ti coordination, while the absorption edge energy  
66 is sensitive to valence (Waychunas 1987; Farges et al. 1996a, 1996b, 1997). In this  
67 study we describe the use of XAFS to observe the coordination and valence state of  
68 synthetically-grown and natural garnets from a wide range of geologic conditions.  
69 Combining XAFS spectroscopy and electron microprobe measurements of Ti content  
70 enables assignment of Ti concentrations to specific crystallographic sites and  
71 provides a platform to discuss the factors influencing Ti solubility and coordination  
72 in garnet.

### 73 **X-ray absorption fine structure**

74 The Ti K-edge X-ray absorption near-edge structure (XANES) pre-  
75 edge feature of the XAFS spectrum is a 1s-3d orbital transition whose normalized  
76 peak height and energy is sensitive to the coordination state of Ti and can be used

77 to differentiate between IV-, V-, and VI-fold Ti (Waychunas 1987; Farges et al.  
78 1996a, 1996b). In materials where Ti exists in multiple coordination states,  
79 residual-minimizing linear combination fitting can accurately predict the relative  
80 contributions of multiple coordination sites to the overall observed signal (Fig. 1).  
81 Additionally, the absorption edge of  $Ti^{3+}$  occurs at a lower energy than that of  $Ti^{4+}$ ,  
82 making it possible to determine if a sample contains multiple valence states of Ti  
83 (Waychunas 1987).

#### 84 **Sample locations**

85  
86 In order to investigate a broad range of garnet-forming environments, this  
87 study examines both synthetically-grown garnets (eclogite- and granulite-facies  
88 conditions) and natural garnet-bearing rocks from low-grade contact metamorphic  
89 rocks to high-grade eclogites and mantle lherzolite xenoliths. Synthetic garnets were  
90 grown in solid-media piston cylinder devices at Rensselaer Polytechnic Institute at  
91 eclogite and granulite facies conditions. The starting materials includes pelite, mid-  
92 ocean ridge basalt and amphibolite bulk compositions with 10 wt. %  $H_2O$  from 800-  
93 900 °C and 1.5-2.5 GPa. Experiments were buffered at the fayalite-magnetite-quartz  
94 (FMQ) buffer using a Pd-foil membrane between the experimental charge and the  
95 buffer (Trail et al. 2012).

96 Natural samples from a wide range of metamorphic facies were analyzed to  
97 observe Ti coordination under conditions where synthetic garnet growth is not  
98 feasible (supplementary material). These natural garnets cover a crystallization  
99 temperature range from 427 to 1000 °C and pressures from 3 to 38 kbar. Garnets  
100 from natural systems also record a wide range of growth histories from primarily

101 peak-metamorphic growth with retrograde metamorphic rims (e.g. garnet from the  
102 Valhalla Metamorphic Complex) to continuous prograde growth (e.g. garnet from  
103 the Fall Mountain nappe).

## 104 **Analytical techniques**

### 105 106 **Microprobe analyses**

107 Wavelength-dispersive X-ray maps for Ti, Fe, Mg, Ca and Mn in garnet were  
108 collected on the Cameca SX100 electron microprobe at RPI prior to analysis at  
109 Brookhaven National Laboratory (BNL), and quantitative analyses were performed  
110 using the analytical routine described in Ackerson et al. (this issue). Due to the low  
111 Ti content of natural garnets, Ti was measured for 300 s on two spectrometers at 15  
112 eV accelerating voltage and 200 nA current, yielding a detection limit near 40 ppm.  
113 Backgrounds of the Ti K-edge peaks at  $\pm 700$  eV were verified using wavelength  
114 dispersive scans above and below the Ti K-edge peak to reduce the possibility of  
115 peak overlap interferences from other elements.  
116

### 117 **XAFS spectral fitting**

118 Synthetic samples were mounted in 2.54 cm epoxy rounds and polished  
119 using 1  $\mu\text{m}$  alumina powder and colloidal silica. Natural samples were prepared as  
120 either thin sections or epoxy rounds for analysis at BNL. XAFS fluorescence and  
121 transmission spectra were collected on beamline X26A at the National Synchrotron  
122 Light Source (NSLS) at BNL. Beamline X26A uses a focused, monochromatic X-ray  
123 source with a  $\sim 0.5$  eV energy resolution ( $\Delta E/E=1E-4$ ). The monochromatic beam is  
124 generated via energy filtering using a channel-cut silicon crystal monochromator cut  
125 along (111). The incident X-ray beam is focused to a  $10 \times 8 \mu\text{m}$  spot which hits the  
126

127 sample at a 45° angle. This produces an effective spot size on the sample of 12x9 μm  
128 with a maximum penetration depth of ~20 μm at the Ti K-edge. All garnet samples  
129 were analyzed in fluorescence mode. In samples where Ti content was low, multiple  
130 spectra were collected and merged with equal weighting to increase the signal to  
131 noise ratio.

132 Possible energy drift was monitored throughout the analytical sessions using  
133 Mg<sup>VI</sup>Ti<sub>2</sub>O<sub>5</sub> powder in transmission mode. Energy drift of the monochromators  
134 occurs as a function of thermal load on the Si crystal due to variations in X-ray flux  
135 over time can affect the relative position of the absorption edge. Drift is a  
136 demonstrated analytical issue for Fe XAFS analysis (Cottrell et al. 2009) who saw  
137 absorption edge drifting up to 0.2 eV over the course of experimentation. Observed  
138 energy drift of the Ti pre-edge feature in this study was very low (standard  
139 deviation of 0.04 eV) and was subsequently disregarded during spectral  
140 comparisons between samples (Supplementary Fig. S1).

#### 141 **XAFS normalization**

142  
143 Normalization of Ti K-edge XAFS spectra to the pre- and post-edge regions  
144 enables concentration-independent comparison of the pre-edge features between  
145 multiple spectra and ultimately determination of Ti coordination in the crystal  
146 lattice. All XAFS data processing was performed using the software program Athena  
147 (Ravel and Newville 2005). The absorption edge for each spectrum was selected by  
148 converting the I<sub>0</sub>-normalized absorption spectrum to first derivative space and  
149 selecting the maximum first derivative of the spectrum within the anticipated edge  
150 region (4982 ± 10 eV). Pre- and post-edge normalization regions were held constant

151 between samples to maintain a reproducible normalization. Pre-edge normalization  
152 was selected from  $-58 \pm 10$  to  $-20 \pm 5$  eV, and the post-edge region from  $114 \pm 15$  to  
153  $212 \pm 5$  eV. The post-edge fitting was performed using a second-order polynomial fit  
154 (Fig. 2). In some samples, low Ti concentrations in garnets resulted in spectra with  
155 erratic, high-noise post-edges that required adjustments to the post-edge fitting  
156 regions. However, changing the pre- and post-edge normalization regions does not  
157 shift the energy of the pre-edge absorption feature. High-noise spectra fitted with  
158 multiple normalization regimes (to assess the impact of normalization on the pre-  
159 edge peak height) resulted in shifts of the normalized pre-edge peak height of less  
160 than 0.1 normalized absorption units.

#### 161 **Selection of analytical spots**

162  
163 In many natural and synthetically-grown garnets, sub-surface Ti-bearing  
164 mineral and/or melt inclusions can contaminate the XAFS spectra. This is a specific  
165 concern in experimental charges, where most garnets contain high densities of  
166 ilmenite and/or rutile inclusions. Beamline X26A is equipped with three energy  
167 dispersive spectrometers (EDS) — one four-element and two single-element vortex  
168 Silicon Drift Detectors from SII NanoTechnology. These detectors can be used  
169 simultaneously to collect 2D composition maps of the analytical regions of interest.  
170 Inclusion-free regions can then be selected for analysis (Fig. 3). See supplementary  
171 information for more details on data reduction and data validation techniques.

#### 172 **Linear combination fitting**

173  
174 Linear combination fitting (LCF) of normalized XAFS spectra was used to  
175 determine the ratio of IV- to VI-fold coordinated Ti in garnets. A synthetic quartz

176 crystal (QTiP-39 from Thomas et al., 2010) and schorlomite from Magnet Cove,  
177 Arkansas (Waychunas 1987; Flohr and Ross 1990) were used as the endmember IV-  
178 and VI-fold spectra, respectively (Fig. 8). Ti in quartz has been observed to occur  
179 entirely in IV-fold coordination (Thomas et al. 2010). Fitting was performed  
180 between 4962-4977 eV using a residual-minimizing technique in Athena. LCF  
181 results were then combined with Ti concentration data from microprobe analyses to  
182 extract <sup>IV</sup>Ti and <sup>VI</sup>Ti concentrations.

183         While the variations in pre-edge peak energy and intensity due to differences  
184 in Ti coordination for end-member (e.g. pure VI-fold Ti) have been established  
185 through multiple investigations(Waychunas 1987; Farges et al. 1996a; Farges  
186 1997), no systematic attempt has been made to quantify coordination ratios in  
187 crystalline samples containing Ti in multiple coordination states. Using simulations  
188 and mechanical mixtures of oxide powders with varying proportions of <sup>IV</sup>Ti, <sup>V</sup>Ti, <sup>VI</sup>Ti,  
189 Farges et al. (1996) demonstrated that mixtures exhibit pre-edge features that are  
190 linear combinations of the end-member spectra. In other words, a 50:50 mixture of  
191 <sup>IV</sup>Ti- and <sup>VI</sup>Ti-bearing glasses produces a pre-edge spectrum that is a convolution of  
192 50% of a pure IV-fold spectrum and 50% of a pure VI-fold spectrum.

### 193 **Selection of <sup>IV</sup>Ti and <sup>VI</sup>Ti standards**

194  
195         Variations in pre-edge spectra due to local bonding environment and  
196 multiple scattering phenomena (Fig. 4) require careful selection of end-member  
197 spectra for accurate linear combination fitting. One of the main uncertainties in  
198 selecting a <sup>IV</sup>Ti end member arises from the fact that no well-characterized garnet  
199 samples (either natural or synthetic) contain only <sup>IV</sup>Ti. This requires a “proxy”

200 spectrum with a well-characterized  $^{IV}Ti$  pre-edge feature. As shown in Figure 4, the  
201 pre-edge peaks for the  $^{IV}Ti$ -bearing quartz and zircon samples analyzed in this  
202 experiment exhibit a similar range of intensities and energies. However, Ti in zircon  
203 exhibits an additional pre-edge peak at higher energy than the primary peak. This  
204 peak does not manifest in quartz spectra or the spectra from garnets with apparent  
205 high  $^{IV}Ti$  content. Additionally, the energy of the pre-edge feature in zircon varies  
206 with orientation, whereas spectral anisotropy does not occur in quartz or garnet.  
207 For these reasons we chose the synthetic quartz crystal QTip-39 (Thomas et al.  
208 2010) as an end-member  $^{IV}Ti$  standard.

209 In contrast to quartz, garnet has a significantly distorted tetrahedral site  
210 (Novak and Gibbs 1971). Whereas tetrahedral site distortion has no significant  
211 impact on pre-edge energy, it can influence the height of the pre-edge peak,  
212 particularly for  $^{VI}Ti$  (Waychunas 1987). The degree to which site distortion on the  
213 tetrahedral site in garnet will influence the  $^{IV}Ti$  peak height is not clear in the  
214 literature. However, the height of the  $^{IV}Ti$  pre-edge feature has been shown to vary  
215 from 0.7 to 1 (Farges et al. 1996a, 1996b, 1997). The quartz spectrum chosen has a  
216 normalized peak height of  $\sim 0.8$  (Fig. 1b) making it possible that fitting garnet  $^{IV}Ti$  to  
217  $^{IV}Ti$  in quartz could result in a minor over- or underestimation of  $^{IV}Ti$  in garnet.  
218 Fitting garnet spectra using the selected quartz standard and several  $^{IV}Ti$  samples  
219 from the literature (Farges et al., 1997) resulted in deviations of calculated  $^{IV}Ti$  on  
220 the order of  $\pm 5\%$ .

221 A natural schorlomite from Magnet Cove, Arkansas was selected as a  
222 representative  $^{VI}Ti$  standard (Waychunas 1987; Flohr and Ross 1990). This sample

223 was selected because of the small full width half maximum (FWHM) of its pre-edge  
224 peak (a small amount of <sup>IV</sup>Ti could result in broadening of this peak; Fig. 1). Also,  
225 Magnet Cove schorlomite has been previously shown to contain entirely <sup>VI</sup>Ti  
226 (Waychunas 1987; Chakhmouradian and McCammon 2005; Antao 2014).

## 227 **Results**

228  
229 In all samples, the absorption edge between analyses was consistent at 4982  
230 ± 0.3 eV, indicating no detectable Ti<sup>3+</sup> (Waychunas 1987). Linear combination fitting  
231 to the pre-edge regions of synthetic and natural garnets demonstrates that Ti can be  
232 incorporated into both the octahedral and tetrahedral sites. All synthetically-grown  
233 garnets have <sup>VI</sup>Ti > 95% (Table 1). Coordination in natural garnets varies between  
234 >90% <sup>IV</sup>Ti and 100% <sup>VI</sup>Ti (supplementary material). LCF fits return low errors  
235 typically less than 2% of the resultant fit. Athena calculates uncertainties (1σ) in  
236 LCFs by multiplying the diagonal of the covariance matrix of the standards by the  
237 square root of the reduced  $\chi^2$  of the fit (defined here as:  $\chi^2 = \frac{\sum(data-fit)^2}{N}$ , where N is  
238 the degrees of freedom). In samples with low Ti and higher noise (e.g. pyrope from  
239 the Dora Maira Massif, sample H11A, Fig. 8) errors can be as high as 5%  
240 (supplementary material).

241 Microprobe analyses of natural garnets yield Ti concentrations ranging from  
242 ~31 ppm in garnets from Mica Creek to over 1100 ppm in garnet from Harpswell  
243 Neck, while synthetic garnets can contain Ti in excess of 2 wt. % TiO<sub>2</sub>.  
244 Concentrations of <sup>IV</sup>Ti and <sup>VI</sup>Ti were calculated by multiplying the weights of IV- and  
245 VI-fold LCF results by Ti content measured by EPMA. Four-coordinated Ti ranges  
246 from below the detection limit (40 ppm) to 192 ppm, while <sup>VI</sup>Ti ranges from near

247 the detection limit to over 1000 ppm. Although the errors on Ca measurements are  
248 typically greater than <sup>VI</sup>Ti concentrations, Ti generally increases with increasing Ca  
249 content of the garnets. No clear relationship exists between Ti and other major  
250 elements. There is no discernible relationship between <sup>IV</sup>Ti with either T or P in  
251 natural garnets, but <sup>VI</sup>Ti increases with increasing Ca and decreasing *T* and *P*.

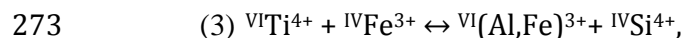
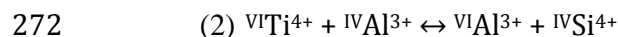
## 252 Discussion

253  
254 Ackerson et al. (this issue) describe Ti substitution and solubility in synthetic  
255 garnets grown at simulated high-grade metamorphic conditions, but the  
256 observations in that study do not necessarily apply to the incorporation of Ti into  
257 garnet in low-mid grade metamorphic systems. In the following discussion we will  
258 show that: (1) Ti in high-grade synthetic garnets is primarily <sup>VI</sup>Ti; (2) minor <sup>IV</sup>Ti  
259 solubility in garnet reflects a T solubility dependence similar to calibrated <sup>IV</sup>Ti  
260 thermobarometers in other minerals; and (3) <sup>VI</sup>Ti in individual garnets across the  
261 entire observed geologic range is linked to <sup>VIII</sup>Ca content.

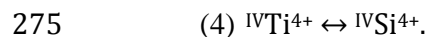
## 262 Limitations of <sup>IV:VI</sup>Ti for thermobarometry

263  
264 Ti K-edge XAFS pre-edge spectra from a suite of natural and synthetic garnets  
265 demonstrate that Ti incorporation occurs on both the octahedral and tetrahedral  
266 sites in garnet. These observations— combined with the major-element trends in  
267 synthetically-grown garnets (Ackerson et al., this issue)— show that Ti  
268 incorporation into garnet involves at least three significant substitution  
269 mechanisms. Octahedral incorporation of Ti likely occurs primarily through three  
270 coupled substitution mechanisms:





274 whereas tetrahedral substitution most likely occurs via:



276 In practical terms  ${}^{\text{IV}}\text{Ti}:$  ${}^{\text{VI}}\text{Ti}$  represents the convolution of multiple substitution  
277 mechanisms operating on several crystallographic sites, making application of  
278 thermodynamically-constrained Ti coordination ratios an ineffective technique for  
279 directly estimating the temperatures and pressures of garnet formation. Changes in  
280  ${}^{\text{IV}}\text{Ti}$  concentrations are relatively minor compared to those of  ${}^{\text{VI}}\text{Ti}$ , and ultimately the  
281 range of Ti coordination-mixing behavior demonstrated in the XAFS spectra is  
282 primarily a reflection of changes in the solubility of  ${}^{\text{VI}}\text{Ti}$ .

283 The concentrations of tetrahedrally-coordinated Ti in garnet are on the same  
284 order of magnitude as other  ${}^{\text{IV}}\text{Ti}$ -bearing silicate minerals [e.g. Ti in quartz (Thomas  
285 et al. 2010), Ti in zircon(Watson and Harrison 2005)]. This is the expected result  
286 given the similarity of the Si tetrahedral sites for which Ti substitutes in these  
287 minerals. As an example, the calculated  ${}^{\text{IV}}\text{Ti}$  content for the interior of garnet V6-B  
288 from the Valhalla Metamorphic Complex is ~85 ppm (820 °C, 8 kbar). Ti-in-quartz  
289 calculations (Thomas et al. 2010) at unity  $a_{\text{TiO}_2}$  for this sample predict a Ti-in-  
290 quartz content of 253 ppm, and Ti-in-zircon estimate 23 ppm in co-crystallizing  
291 zircon (Ferry and Watson 2007). Ultimately, the low concentrations of  ${}^{\text{IV}}\text{Ti}$  and  
292 associated high errors in both EPMA analyses and XAFS spectral fits hinder any  
293 practical thermobarometric calibrations of  ${}^{\text{IV}}\text{Ti}$ .

294 **Ti coordination in synthetic garnet**

295  
296 Garnets crystallized in multiple bulk compositions over a range of eclogite-  
297 and granulite-facies temperatures and pressures (buffered at the FMQ oxygen  
298 fugacity buffer) contain up to several wt. % TiO<sub>2</sub>. Major-element trends in these  
299 garnets suggest Ti is incorporated primarily on the octahedral site (Ackerson et al.,  
300 this issue). Linear combination fitting of the pre-edge peaks of all synthetic garnets  
301 supports the major-element trends, returning fits over 98% <sup>VI</sup>Ti (Fig. 6) for almost  
302 all garnets. <sup>VI</sup>Ti is between 95 and 98% in several garnets, suggesting either  
303 multiple-scattering events are broadening the pre-edge peak relative to the <sup>VI</sup>Ti  
304 standard, or a minor contribution of <sup>IV</sup>Ti. Given the errors in the linear combination  
305 fits are around 1-1.5%, it is difficult to assign <sup>IV</sup>Ti concentrations to the experiments.  
306 The fact that there is no discernible <sup>IV</sup>Ti suggests <sup>IV</sup>Ti concentrations in the synthetic  
307 garnets are at most several hundred ppm.

308 **Examples from nature**

309  
310 The coordination behavior observed in synthetic garnets aligns with the Ti  
311 coordination and substitution mechanisms observed through major-element  
312 chemical trends (Ackerson et al., this issue). However, growth of synthetic garnets  
313 is limited to temperatures and pressures greater than experienced by most natural  
314 garnets. Furthermore, the synthetic garnets were grown at static T and P and do not  
315 record the range of prograde and retrograde histories recorded in many natural  
316 garnets. We analyzed Ti coordination in natural garnets from a range of conditions  
317 (low-grade contact metamorphism to mantle conditions) to assess whether the  
318 observations made in the synthetic garnets can be applied to garnets from a range of

319 natural conditions. Furthermore, by observing core-rim XAFS transects of garnets  
320 with well-characterized metamorphic histories, we can observe the interplay  
321 between  $T$ ,  $P$  and composition on Ti solubility and coordination in garnet.

322  
323 **Harpwell Neck** Sample 96-1 is a garnet-grade schist from the Jewel  
324 Formation in Harpswell, Maine. Garnets from this formation have been the topic of  
325 considerable discussion as to whether garnet porphyroblasts form from the  
326 coalescence of multiple garnet nuclei (Daniel and Spear 1998; Spear and Daniel  
327 2001) or nucleation of a single garnet around a Mn-rich precursor mineral phase  
328 (Hirsch et al. 2003).

329 Core-rim variations in Fe, Mg and Mn in garnets from sample 96-1 indicate  
330 equilibrium, prograde garnet growth. Ca zoning does not match the zoning patterns  
331 of the other major elements and suggests disequilibrium Ca incorporation along an  
332 isobaric heating path due to garnet growth outpacing diffusive Ca replenishment to  
333 the mineral-matrix interface (Spear and Daniel 2001). Ti in these garnets is almost  
334 entirely VI-fold ( $^{IV}\text{Ti}$  content is near the detection limit of the technique as applied at  
335 beamline X26A), and variations in Ti concentration trend with Ca (Fig. 7). The  
336 correlation between Ti and Ca suggests that either Ti replenishment to the garnet-  
337 matrix interface is kinetically similar to Ca replenishment or Ti solubility in garnet is  
338 influenced primarily by the grossular content.

339 The effect of  $T$  and  $P$  on Ti incorporation in sample 96-1 is difficult to  
340 ascertain. Given that the prevailing petrogenetic theory for garnet growth in this  
341 sample assumes isobaric heating, pressure likely did not directly influence Ti  
342 solubility. Temperature is modeled to increase throughout garnet growth, yet Ti

343 does not display a systematically constant increase or decrease from core to rim.  
344 These observations support the notion that garnet composition (in particular the  
345 grossular content) have a large influence on <sup>VI</sup>Ti solubility, and compositional  
346 variations exert greater control over the <sup>VI</sup>Ti than *T* and *P* over the garnet  
347 crystallization interval.

348         **Nelson Aureole** The Nelson contact aureole provides another example of the  
349 influence of Ca content on Ti concentration in garnet. The Nelson aureole is a pelitic  
350 contact metamorphic aureole surrounding the Jurassic-aged Nelson Batholith. The  
351 contact aureole is characterized by an isobaric (3.5 kbar), pluton-ward increasing  
352 metamorphic grade defined by mineral-in reactions— from garnet-in reactions at  
353 527 °C to K-feldspar-in reactions at 653 °C (Pattison and Vogl 2005; Pattison and  
354 Tinkham 2009). In the present study we analyzed garnets from the garnet-in,  
355 staurolite-in, (557 °C), andalusite-in (560 °C) and K-feldspar-in zones.

356         As an example of the effect of Ca on Ti uptake, we note that garnets from  
357 sample 93CW22 of Pattison and Tinkham, 2009 from the andalusite-in zone exhibit  
358 Ca zoning patterns similar to those expressed in garnet from Harpswell Neck. The  
359 garnets have increasing rimward Ca content to an abrupt low Ca rim (Fig. 8). Like  
360 Harpswell Neck, these garnets are believed to form through isobaric, increasing  
361 temperature prograde growth. The interior of these garnets likely formed through  
362 the reaction *muscovite + chlorite + quartz = garnet + biotite + H<sub>2</sub>O*, while the  
363 low-Ca rim formed through *muscovite + staurolite + quartz = andalusite +*  
364 *garnet + biotite + H<sub>2</sub>O*. The low-Ca rim is thought to form via the shift to an  
365 andalusite-forming reaction creating a new equilibrium assemblage with a lower

366 grossular activity (Pattison and Vogl 2005; Pattison and Tinkham 2009). All of these  
367 reactions occur at rutile saturation, indicating constant unity  $a_{TiO_2}$  throughout  
368 garnet crystallization. Composition maps again reveal the influence of grossular  
369 content on Ti incorporation in garnet and bolster the notion that Ti content is  
370 influenced by grossular content over the garnet crystallization interval (Fig. 8).

371 **Valhalla Metamorphic Complex and retrograde equilibration** Garnets  
372 from the Valhalla Metamorphic Complex crystallized at peak metamorphic  
373 conditions around 820 °C and 8 kbar after which they experienced a complex  
374 retrograde re-equilibration path during exhumation to the surface (Hallett and  
375 Spear 2011; Spear 2004; Spear and Parrish 1996). Garnets in the paragneisses were  
376 subject to retrograde net-transfer reactions that resulted in garnet consumption.  
377 Core-rim variations in Fe/(Fe+Mg) help constrain the cooling rates and exhumation  
378 history of the region. Retrograde equilibration near garnet rims is demonstrated in  
379 the rimward decrease in Mg and increase in Fe. The XAFS pre-edge spectra of Ti in  
380 sample V6B reflect this retrograde re-equilibration. Octahedral Ti is relatively  
381 constant across most of the grain, but increases near the rim of the garnet (Fig. 9).  
382 As with the examples above, this increase coincides with a marked increase in Ca  
383 content.

384 While the rimward increase in  $^{VI}Ti$  reflects a retrograde increase in Ca,  $^{IV}Ti$   
385 decreases toward the rim. The decrease in  $^{IV}Ti$  within the re-equilibrated zone can  
386 occur either as a function of the changing garnet composition or a decrease in  
387 solubility as a function of changes in T or P. Given that  $^{IV}Ti$  substitutes directly for Si  
388 (as opposed to requiring a coupled substitution), changes in dodecahedral or

389 octahedral element substitutions are unlikely to influence  $^{IV}\text{Ti}$  solubility. The  
390 notable exception to this is  $^{IV}\text{Al}^{3+}$ , where appreciable  $^{IV}\text{Al}^{3+}$  solubility could influence  
391 the solubility of Ti on the tetrahedral site, although cation-normalization of the  
392 garnet formula for sample V6B show no evidence of appreciable  $^{IV}\text{Al}$  solubility.

393         The retrograde rim on garnet V6B may provide insight into the influence of  $T$   
394 and  $P$  on  $^{IV}\text{Ti}$  solubility. If  $^{IV}\text{Ti}$  solubility in garnet behaves like experimentally-  
395 calibrated trace element thermobarometers,  $^{IV}\text{Ti}$  solubility will increase with  
396 temperature and decrease with increasing pressure (Thomas et al. 2010).  
397 Retrogression occurs via a decrease in both temperature and pressure. If decreasing  
398 pressure had a greater effect on  $^{IV}\text{Ti}$  solubility than decreasing temperature,  $^{IV}\text{Ti}$   
399 would increase in the retrograde rim. The fact that  $^{IV}\text{Ti}$  increases in the rim suggests  
400 that either temperature has a greater control on  $^{IV}\text{Ti}$  solubility in garnet than  
401 pressure, or  $^{IV}\text{Ti}$  decreases with decreases in both  $T$  and  $P$ .

402         **Fall Mountain Nappe** The Fall Mountain nappe is a thrust system along the  
403 New Hampshire-Vermont border where thrusting emplaced a regionally-  
404 metamorphosed (upper) pelitic rock atop another (lower) pelitic rock. Whereas the  
405 garnets from Harpswell Neck and Nelson Aureole experienced isobaric prograde  
406 metamorphism, the lower unit of the Fall Mountain nappe experienced near-  
407 isothermal prograde metamorphism through loading via emplacement of the upper  
408 unit of the nappe (Spear, Hickmott, and Selverstone 1990). Sample BF-18C is a  
409 staurolite-kyanite grade garnet, biotite, chlorite, muscovite, plagioclase and quartz-  
410 bearing schist from the lower plate of the nappe complex. Modeling of zoning in  
411 garnet from BF-18C suggests prograde growth from  $\sim 3.2$  kbar and  $\sim 450$  °C to  $\sim 5.3$

412 kbar and 500 °C. Tetrahedral Ti does not change significantly across the garnet,  
413 while <sup>VI</sup>Ti decreases with prograde growth (Fig. 10). The decrease in <sup>VI</sup>Ti could  
414 represent a decrease in solubility with increasing temperature and pressure, but the  
415 effect is difficult to deconvolve from the effect of decreasing Ca content.

#### 416 **Comparison between natural and synthetic garnets**

417

418 Combining <sup>VI</sup>Ti concentration data from natural garnets with that of  
419 synthetically grown garnets affords the opportunity to observe Ti in garnets over  
420 almost the entire range of crustal geologic conditions— from shallow crustal contact  
421 metamorphism to UHT and UHP conditions present in the lower crust and upper  
422 mantle. Comparing the natural and synthetic garnet databases gives some insight  
423 into the factors influencing Ti solubility in garnet, and support the notion that <sup>VI</sup>Ti  
424 solubility is strongly influenced by grossular content.

425 There is a general increase in pyrope and decrease in almandine content with  
426 temperature over the range of both synthetic and natural samples (Fig. 11a,b).  
427 These relatively constant trends are not reflected in the Ti content, which has a  
428 distinct gap between the natural and synthetic garnets in temperature, pressure,  
429 pyrope and almandine space. Titanium content generally decreases with increasing  
430 *T* and *P* in natural garnets (Fig. 12a,b). However, Ti demonstrates a near-constant  
431 increase with increasing grossular content (Fig. 11c, Fig. 12c). Ultimately, there is a  
432 stronger correlation with Ti and  $X_{\text{grs}}$  than with *T*, *P*,  $X_{\text{alm}}$  or  $X_{\text{pyr}}$ .

#### 433 **High-grade natural garnets and rutile exsolution**

434

435 Garnets from high-grade continental metamorphic and mantle sources serve  
436 as representations of the interplay between *T*, *P*, and composition at elevated

437 temperatures and pressures and again demonstrate the effect of garnet chemistry  
438 on Ti incorporation. Coesite-bearing pyrope garnets from ultra-high pressure (UHP)  
439 Mg-rich metapelites of Dora Maira Central Massif experienced peak metamorphic  
440 growth at 800 °C and 37 kbar pressure (Schertl et al. 1991). Dora Maira garnets  
441 analyzed in this study are almost entirely pyrope, and despite crystallizing in the  
442 presence of rutile ( $a_{TiO_2} = 1$ ) contain less than 40 ppm Ti. In contrast, synthetically-  
443 grown garnets from metapelitic bulk compositions at 800 °C and 35 kbar contain  
444 ~10 wt. % CaO and 1.2 wt. % TiO<sub>2</sub> (sample C-3155 from Tailby, 2009). The presence  
445 of intact coesite and a lack of crystallographically-aligned exsolved rutile needles in  
446 Dora Maira pyrope crystals suggest it is unlikely the garnets would have undergone  
447 complete retrograde diffusive re-equilibration of Ti, and that Ti in these garnets is  
448 near the primary crystallization composition.

449         The low Ti content of Dora Maira garnets yield noisy pre-edge spectra (Fig.  
450 13), but these spectra indicate that Ti is almost entirely in VI-fold coordination.  
451 Compared with garnets from Valhalla that grew at similar temperatures, the lack of  
452 <sup>IV</sup>Ti in Dora Maira garnet suggests an inverse relationship between pressure and <sup>IV</sup>Ti  
453 incorporation.

454         The low solubility of <sup>VI</sup>Ti is in marked contrast to other UHP/UHT terranes  
455 where oriented rutile needles in garnets have been suggested as possible UHP/UHT  
456 indicators in garnet peridotites and eclogites (Van Roermund et al. 2000; Mposkos  
457 and Kostopoulos 2001; Zhang et al. 2003; Ague et al. 2013). In terms of Ti content of  
458 garnet, the main difference between rutile-bearing and rutile-absent UHP/UHT  
459 rocks is garnet composition. For example, garnets from eclogites of the Sulu UHP



485 temperature or pressure. Solubility and variations therein of <sup>IV</sup>Ti in the suite of  
486 natural garnets indicate that <sup>IV</sup>Ti obeys similar trends to <sup>IV</sup>Ti in other minerals (e.g.  
487 Ti in quartz, Ti in zircon). Changes in Ti coordination and <sup>IV</sup>Ti and <sup>VI</sup>Ti solubility  
488 within garnets can be used to interpret geochemical events during garnet growth.  
489 This study is limited by intrinsic errors in P and T estimates for natural systems, and  
490 correlation between Ti and Ca in garnets (e.g. Harpswell Neck) suggest coupled  
491 disequilibrium incorporation in some samples. Better constraints on garnet growth  
492 conditions in the studied samples using modern thermobarometric techniques  
493 could serve to increase the efficacy and utility of Ti in garnet calibrations. Also,  
494 better constraints on the chemical and mechanical properties of Ti end member  
495 garnets could aid in thermodynamic modeling of the activities of system  
496 components over the assumed *T* and *P* intervals of garnet growth and could inform  
497 the underlying chemical processes involved in <sup>VI</sup>Ti incorporation. Ultimately this  
498 could lead to the development of a thermodynamically-constrained <sup>VI</sup>Ti  
499 thermobarometer.

### 500 **Acknowledgments**

501  
502 We would like to thank Sue Wirick, Bill Rao, and Tony Lanzirotti at beamline  
503 X26A located at the National Synchrotron Light Source (NSLS) for help in collecting  
504 and interpreting the XANES data used in this study. The X26A beamline is supported  
505 by DoE grant DE-FG02-92ER14244 funded through the University of Chicago. The  
506 NSLS is supported by DoE grant DE-AC02-98CH10886. Thanks also to Frank Spear,  
507 Dave Pattison and Mike Howard for allowing us to analyze their garnet samples.  
508 Thanks to Dustin Trail, Jay Thomas and Danielle Cherniak for discussion during the

509 development of this project. Much of this work was funded through NSF-EAR grant  
510 0948204.

511

512

## References

513

514 Ague, J.J., and Eckert, J.O. (2012) Precipitation of rutile and ilmenite needles in  
515 garnet: Implications for extreme metamorphic conditions in the Acadian  
516 Orogen, U.S.A. *American Mineralogist*, 97, 840–855.

517 Ague, J.J., Eckert, J.O., Chu, X., Baxter, E.F., and Chamberlain, C.P. (2013) Discovery of  
518 ultrahigh-temperature metamorphism in the Acadian orogen, Connecticut,  
519 USA. *Geology*, 41, 271–274.

520 Antao, S.M. (2014) Schorlomite and morimotoite: what's in a name? *Powder*  
521 *Diffraction*, 29, 346–351.

522 Bishop, F.C., Smith, J.V., and Dawson, J.B. (1978) Na, K, P and Ti in garnet, pyroxene  
523 and olivine from peridotite and eclogite xenoliths from African kimberlites.  
524 *Lithos*, 11, 155–173.

525 Chakhmouradian, A.R., and McCammon, C.A. (2005) Schorlomite: a discussion of the  
526 crystal chemistry, formula, and inter-species boundaries. *Physics and*  
527 *Chemistry of Minerals*, 32, 277–289.

528 Cottrell, E., Kelley, K.A., Lanzirrotti, A., and Fischer, R.A. (2009) High-precision  
529 determination of iron oxidation state in silicate glasses using XANES.  
530 *Chemical Geology*, 268, 167–179.

531 Daniel, C.G., and Spear, F.S. (1998) Three-dimensional patterns of garnet nucleation  
532 and growth. *Geology*, 26, 503.

533 Ene, V.V., and Schulze, D.J. (2013) Major and trace element geochemistry of ilmenite  
534 suites from the Kimberley diamond mines, South Africa. *AGU Fall Meeting*  
535 *Abstracts*, 23, 2765.

536 Farges, F. (1997) Coordination of Ti<sup>4+</sup> in silicate glasses: A high-resolution XANES  
537 spectroscopy study at the Ti K edge. *Amer. Mineral.*, 82, 36–43.

538 Farges, F., Brown Jr., G.E., Navrotsky, A., Gan, H., and Rehr, J.J. (1996a) Coordination  
539 chemistry of Ti(IV) in silicate glasses and melts: II. Glasses at ambient  
540 temperature and pressure. *Geochimica et Cosmochimica Acta*, 60, 3039–  
541 3053.

- 542 Farges, F., Brown Jr., G.E., and Rehr, J.J. (1996b) Coordination chemistry of Ti(IV) in  
543 silicate glasses and melts: I. XAFS study of titanium coordination in oxide  
544 model compounds. *Geochimica et Cosmochimica Acta*, 60, 3023–3038.
- 545 Farges, F., Brown, G.E., and Rehr, J.J. (1997) Ti K-edge XANES studies of Ti  
546 coordination and disorder in oxide compounds: Comparison between theory  
547 and experiment. *Physical Review B*, 56, 1809–1819.
- 548 Ferry, J.M., and Watson, E.B. (2007) New thermodynamic models and revised  
549 calibrations for the Ti-in-zircon and Zr-in-rutile thermometers. *Contributions  
550 to Mineralogy and Petrology*, 154, 429–437.
- 551 Flohr, M.J.K., and Ross, M. (1990) Alkaline igneous rocks of Magnet Cove, Arkansas:  
552 Mineralogy and geochemistry of syenites. *Lithos*, 26, 67–98.
- 553 Hallett, B.W., and Spear, F.S. (2011) Insight into the cooling history of the Valhalla  
554 complex, British Columbia. *Lithos*, 125, 809–824.
- 555 Hirsch, D.M., Prior, D.J., and Carlson, W.D. (2003) An overgrowth model to explain  
556 multiple, dispersed high-Mn regions in the cores of garnet porphyroblasts.  
557 *The American mineralogist*, 88, 131–141.
- 558 Hwang, S.L., Yui, T.F., Chu, H.T., Shen, P., Schertl, H.P., Zhang, R.Y., and Liou, J.G.  
559 (2007) On the origin of oriented rutile needles in garnet from UHP eclogites.  
560 *Journal of Metamorphic Geology*, 25, 349–362.
- 561 Mposkos, E.D., and Kostopoulos, D.K. (2001) Diamond, former coesite and  
562 supersilicic garnet in metasedimentary rocks from the Greek Rhodope: a new  
563 ultrahigh-pressure metamorphic province established. *Earth and Planetary  
564 Science Letters*, 192, 497–506.
- 565 Novak, G.A., and Gibbs, G.V. (1971) The crystal chemistry of the silicate garnets.  
566 *American Mineralogist*, 56, 791–825.
- 567 Pattison, D.R.M., and Tinkham, D.K. (2009) Interplay between equilibrium and  
568 kinetics in prograde metamorphism of pelites: an example from the Nelson  
569 aureole, British Columbia. *Journal of Metamorphic Geology*, 27, 249–279.
- 570 Pattison, D.R.M., and Vogl, J.J. (2005) Contrasting Sequences of Metapelitic Mineral-  
571 Assemblages in the Aureole of the Tilted Nelson Batholith, British Columbia:  
572 Implications for Phase Equilibria and Pressure Determination in Andalusite-  
573 Sillimanite-Type Settings. *The Canadian Mineralogist*, 43, 51–88.
- 574 Proyer, A., Habler, G., Abart, R., Wirth, R., Krenn, K., and Hoinkes, G. (2013) TiO<sub>2</sub>  
575 exsolution from garnet by open-system precipitation: evidence from  
576 crystallographic and shape preferred orientation of rutile inclusions.  
577 *Contributions to Mineralogy and Petrology*, 166, 211–234.

- 578 Ravel, B., and Newville, M. (2005) ATHENA, ARTEMIS, HEPHAESTUS : Data analysis  
579 for X-ray absorption spectroscopy using IFEFFIT. *Journal of synchrotron*  
580 *radiation*, 12, 537–541.
- 581 Schertl, H.-P., Schreyer, W., and Chopin, C. (1991) The pyrope-coesite rocks and their  
582 country rocks at Parigi, Dora Maira Massif, Western Alps: detailed  
583 petrography, mineral chemistry and PT-path. *Contributions to Mineralogy*  
584 *and Petrology*, 108, 1–21.
- 585 Snoeyenbos, D.R., Williams, M.L., and Hanmer, S. (1995) Archean high-pressure  
586 metamorphism in the western Canadian Shield. *European Journal of*  
587 *Mineralogy*, 7, 1251–1272.
- 588 Spear, F.S. (2004) Fast Cooling and Exhumation of the Valhalla Metamorphic Core  
589 Complex, Southeastern British Columbia. *International Geology Review*, 46,  
590 193–209.
- 591 Spear, F.S., and Daniel, C.G. (2001) Diffusion control of garnet growth, Harpswell  
592 Neck, Maine, USA. *Journal of Metamorphic Geology*, 19, 179–195.
- 593 Spear, F.S., and Parrish, R.R. (1996) Petrology and Cooling Rates of the Valhalla  
594 Complex, British Columbia, Canada. *Journal of Petrology*, 37, 733–765.
- 595 Spear, F.S., Hickmott, D.D., and Selverstone, J. (1990) Metamorphic consequences of  
596 thrust emplacement, Fall Mountain, New Hampshire. *Geological Society of*  
597 *America Bulletin*, 102, 1344–1360.
- 598 Tailby, N.D. (2009) New experimental techniques for studying: (i) trace element  
599 substitution in minerals, and (ii) determining S-L-V relationships in silicate-  
600 H<sub>2</sub>O systems at high pressure. Australian National University.
- 601 Thomas, J.B., Watson, E.B., Spear, F.S., Shemella, P.T., Nayak, S.K., and Lanzirrotti, A.  
602 (2010) TitaniQ under pressure: the effect of pressure and temperature on the  
603 solubility of Ti in quartz. *Contributions to Mineralogy and Petrology*, 160,  
604 743–759.
- 605 Trail, D., Watson, E.B., and Tailby, N.D. (2012) Ce and Eu anomalies in zircon as  
606 proxies for the oxidation state of magmas. *Geochimica et Cosmochimica Acta*,  
607 97, 70–87.
- 608 Tropper, P., Konzett, J., and Finger, F. (2005) Experimental constraints on the  
609 formation of high-P/high-T granulites in the Southern Bohemian Massif.  
610 *European Journal of Mineralogy*, 17, 343–356.
- 611 Van Roermund, H.L.M., Drury, M.R., Barnhoorn, A., and De Ronde, A. (2000) Non-  
612 silicate inclusions in garnet from an ultra-deep orogenic peridotite.  
613 *Geological Journal*, 35, 209–229.

- 614 Watson, E.B., and Harrison, T.M. (2005) Zircon Thermometer Reveals Minimum  
615 Melting Conditions on Earliest Earth. *Science*, 308, 841–844.
- 616 Waychunas, G.A. (1987) Synchrotron radiation XANES spectroscopy of Ti in  
617 minerals: Effects of Ti bonding distances, Ti valence, and site geometry on  
618 absorption edge structure. *American Mineralogist*, 72, 89–101.
- 619 Zhang, R.Y., Zhai, S.M., Fei, Y.W., and Liou, J.G. (2003) Titanium solubility in  
620 coexisting garnet and clinopyroxene at very high pressure: the significance of  
621 exsolved rutile in garnet. *Earth and Planetary Science Letters*, 216, 591–601.
- 622 Zhang, R.Y., Liou, J.G., Zheng, J.-P., Griffin, W.L., Yui, T.-F., and O'Reilly, S.Y. (2005)  
623 Petrogenesis of the Yangkou layered garnet-peridotite complex, Sulu UHP  
624 terrane, China. *American Mineralogist*, 90, 801–813.

625

626

### List of Figure Captions

627

628 **Figure 1:** Typical Ti K-edge XAFS spectra for <sup>IV</sup>Ti and <sup>VI</sup>Ti. (a) XAFS spectra for <sup>IV</sup>Ti  
629 from quartz QTIP-39 (blue) and <sup>VI</sup>Ti from a schorlomite garnet from Magnet Cove,  
630 Arkansas (red) have pre-edge features (b) at different normalized absorptions and  
631 energies. (c) Combinations of the two coordination states result in spectra that are  
632 linear combinations of the two end-members.

633 **Figure 2:** Normalizing a <sup>VI</sup>Ti XAFS spectrum of schorlomite from Magnet Cove, with  
634 absorption expressed as  $[\mu(E)]$ . (a) The height of the edge step absorption is  
635 proportional to the X-ray flux and Ti concentration in the sample. (b) Normalization  
636 of spectra by selecting the pre- and post-edge normalization regions and selecting  
637 the absorption edge allows for (c) concentration-independent comparison of  
638 spectra to an edge step of 1.

639 **Figure 3:** Compositional mapping of a synthetic garnet from sample 8-GLOSS. Fly  
640 scan imaging enables selection of inclusion-free zones within garnets. In this  
641 example, (a) Fe and (b) Ca maps help distinguish between seed garnets and new

642 garnet growth, while (c) Ti maps indicate the locations of Ti-rich inclusions. Field of  
643 view is 250X250  $\mu\text{m}$  at 5  $\mu\text{m}/\text{pixel}$  with a dwell time of 2 ms.

644 **Figure 4:** Pre-edge features of multiple minerals analyzed in this study. Spectra are  
645 offset for ease of comparison. (a)  $^{\text{VI}}\text{Ti}$  in a suite of silicate and oxide minerals show  
646 various contributions of the three pre-edge peaks described by Waychunas, 1987.  
647 (b)  $^{\text{IV}}\text{Ti}$  of zircon and quartz. The energy of the pre-edge peak in zircon is dependent  
648 on the crystal orientation relative to the polarization vector of the incident beam.

649 **Figure 5:** Linear combination fitting of the pre-edge spectrum of sample H11A with  
650 end-member  $^{\text{VI}}\text{Ti}$  and  $^{\text{IV}}\text{Ti}$ .

651 **Figure 6:** Pre-edge spectra of synthetically-grown garnets suggest Ti is almost  
652 entirely VI-fold coordinated.

653 **Figure 7:** Garnets in sample 96-1 from Harpswell Neck. (a,b,c) Garnets exhibit core-  
654 rim variations in all major elements. (d) Core-rim combined XAFS and EPMA  
655 analyses of garnet show little variation in the coordination of garnet from core to  
656 rim, but  $^{\text{VI}}\text{Ti}$  concentrations change concomitantly with changes in Ca content.

657 **Figure 8:** Garnet from sample 93CW22 of the Nelson aureole. (a-e) Composition  
658 maps showing correlation between Ca and Ti. (f) Results of XAFS pre-edge fitting  
659 demonstrate near-constant Ti coordination throughout the garnet.

660 **Figure 9:** Garnet from sample V6B from the Valhalla Metamorphic Complex. (a,b,c)  
661 Major-element composition maps displaying chemically uniform cores and  
662 retrogressed rims. (d) XAFS and EPMA core-rim transects show a rim-ward  
663 decrease in  $^{\text{IV}}\text{Ti}$  and increase in  $^{\text{VI}}\text{Ti}$ .

664 **Figure 10:** Garnet from sample BF18C from the lower unit of the Fall Mountain  
665 nappe exhibiting prograde growth.  $^{IV}Ti$  is relatively constant from core-rim, while  
666  $^{VI}Ti$  content decreases with prograde growth and decreasing Ca.  
667 **Figure 11:**  $^{VI}Ti$  versus  $T$  and (a)  $X_{alm}$ , (b)  $X_{pyr}$ , and (c)  $X_{grs}$ .  
668 **Figure 12:**  $^{VI}Ti$  versus  $T$  and  $X_{grs}$ .  
669 **Figure 13:** Pre-edge spectra for pyrope-rich high  $T$  and high  $P$  garnets,  
670 demonstrating Ti incorporation is almost entirely octahedral.  
671

672  
673

## Tables

**Table 1:** Results of linear combination fitting of Ti XAFS pre-edge features in synthetic garnets from Ackerson et al., this issue.

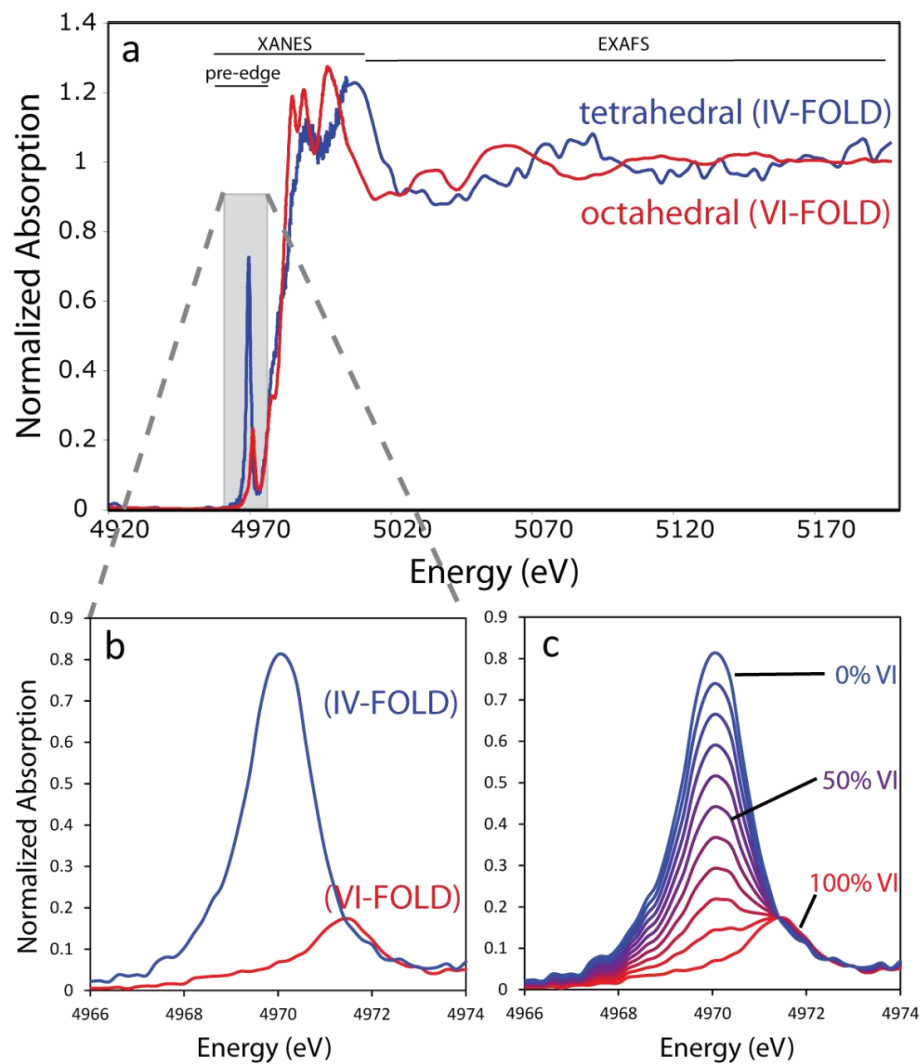
Sample #	10-GLOSS	9-GLOSS	15-AMPH	15-GLOSS	15-MORB	13-GLOSS
T (°C)	800	900	800	800	800	850
P (GPa)	15	15	25	25	25	25
% IV-fold	1.0	11.0	3.0	0.0	2.0	0.0
% VI-fold	99.0	89.0	97.0	100.0	98.0	100.0
model error (%)	1.0	2.0	1.0	0.0	1.0	0.0
Sample #	14-GLOSS	14-MORB	C-3119	D-1011	D-1069	
T (°C)		900	900	900	900	750
P (GPa)		25	25	35	25	35
% IV-fold		4.0	4.0	0.0	10.0	5.0
% VI-fold		96.0	96.0	100.0	90.0	95.0
model error (%)		1.0	1.0	1.0	2.0	2.0

674

675  
676  
677

## Figures

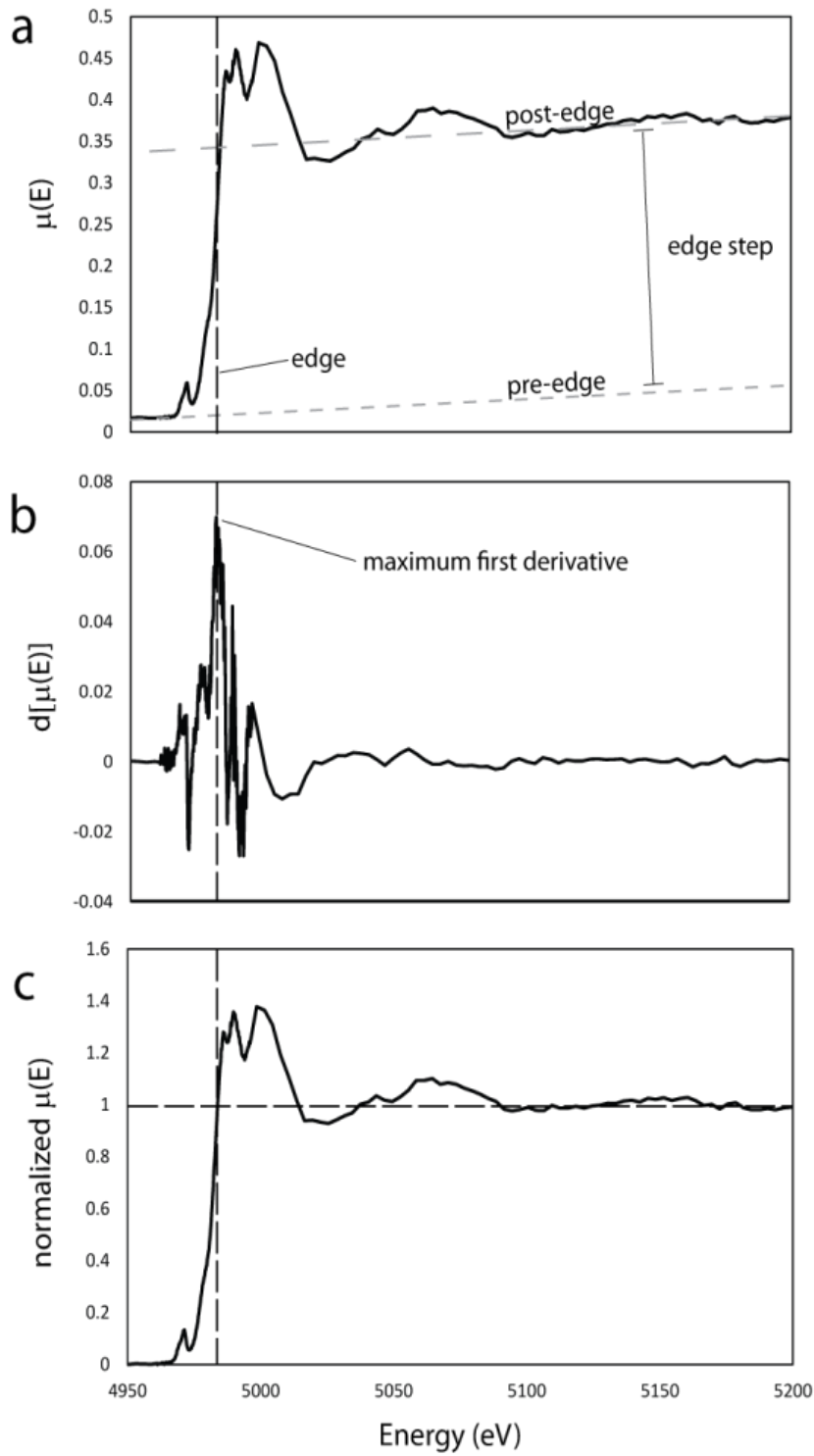
Figure 1



678

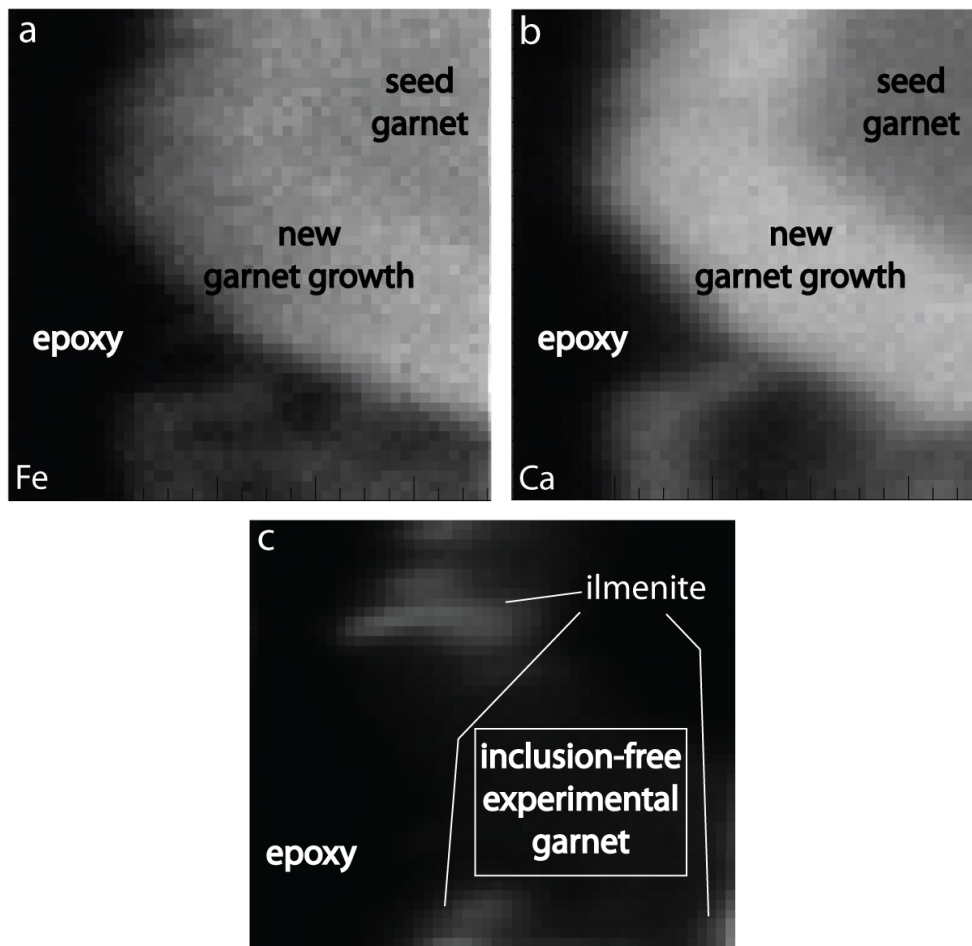
679

680 **Figure 2**



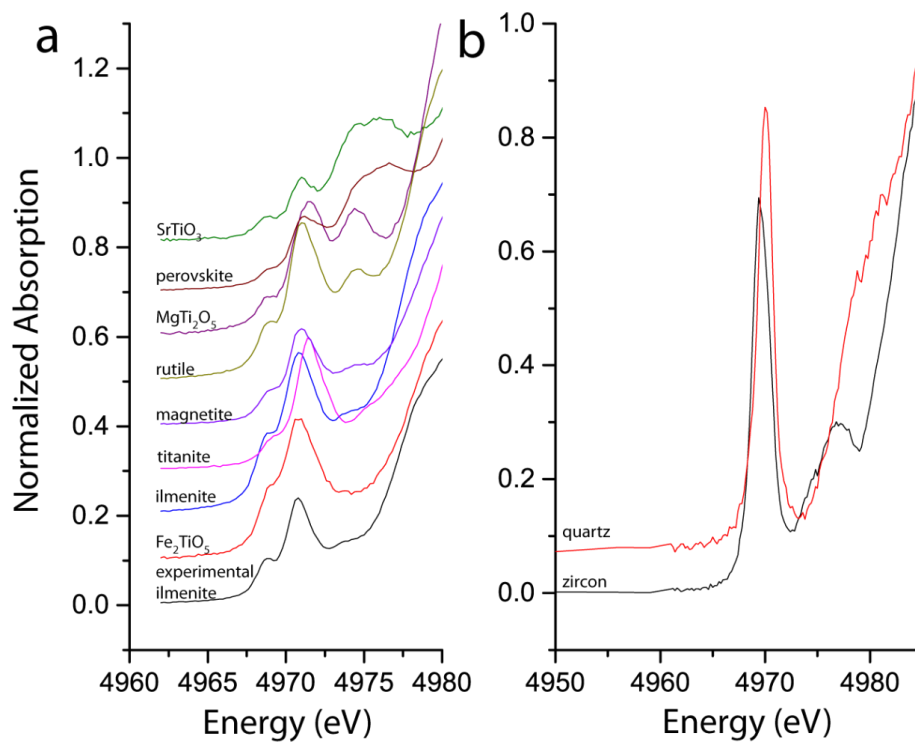
681

682 **Figure 3**



683

684 **Figure 4**

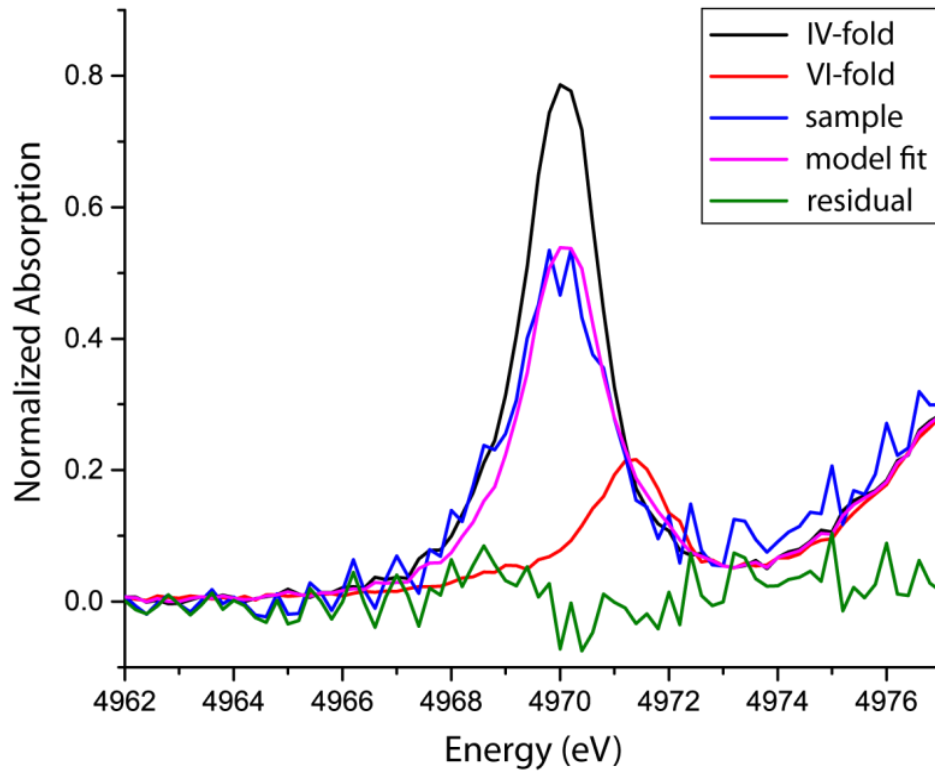


685

686

687

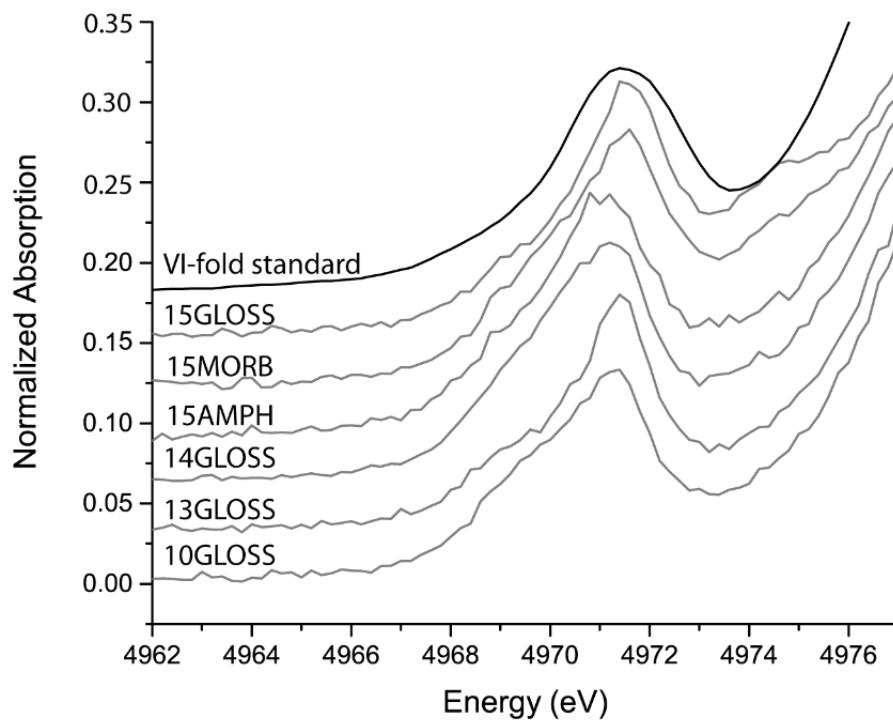
688 **Figure 5**



689

690

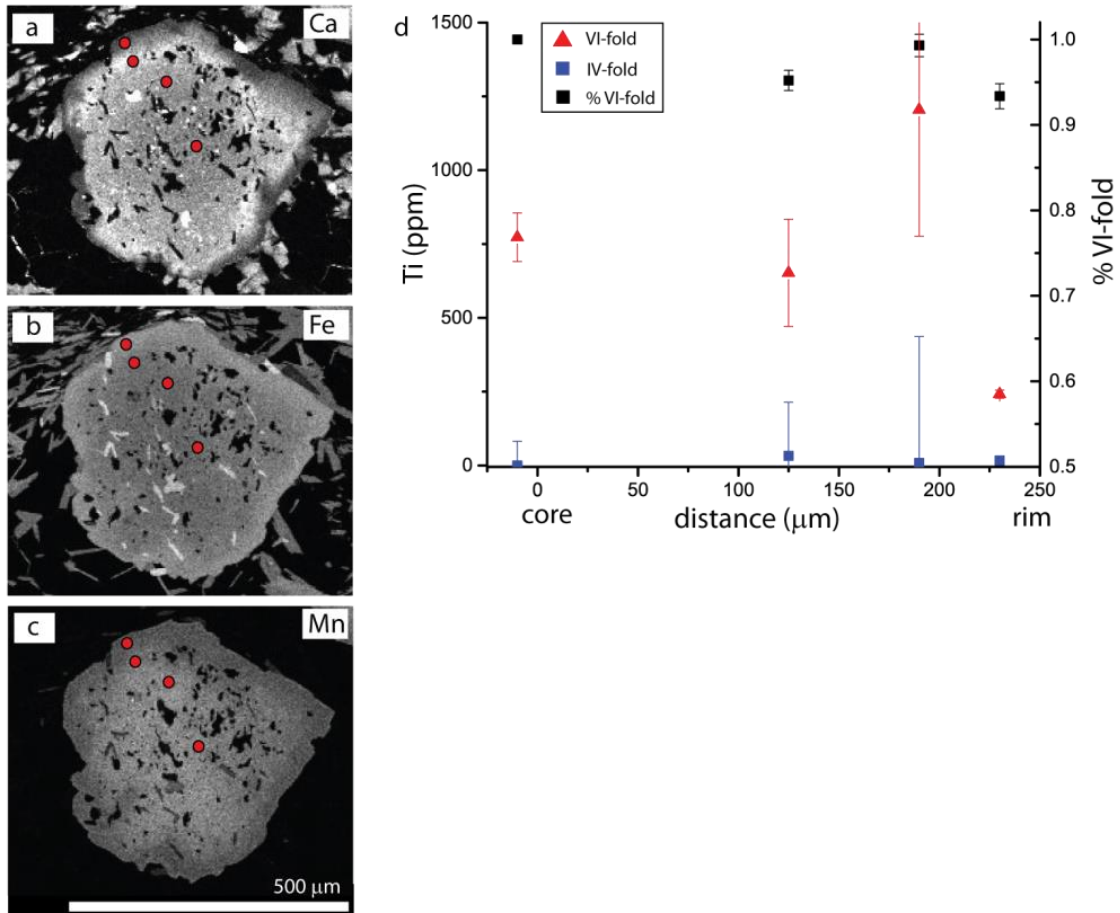
691 **Figure 6**



692

693

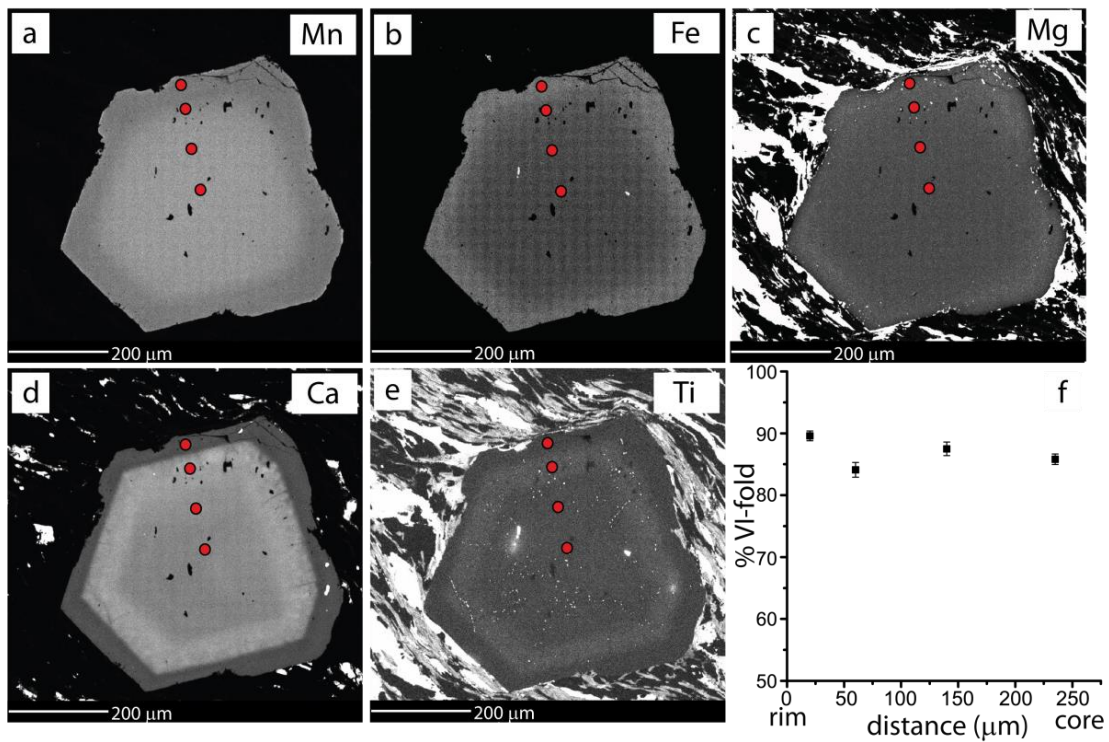
694 **Figure 7**



695

696

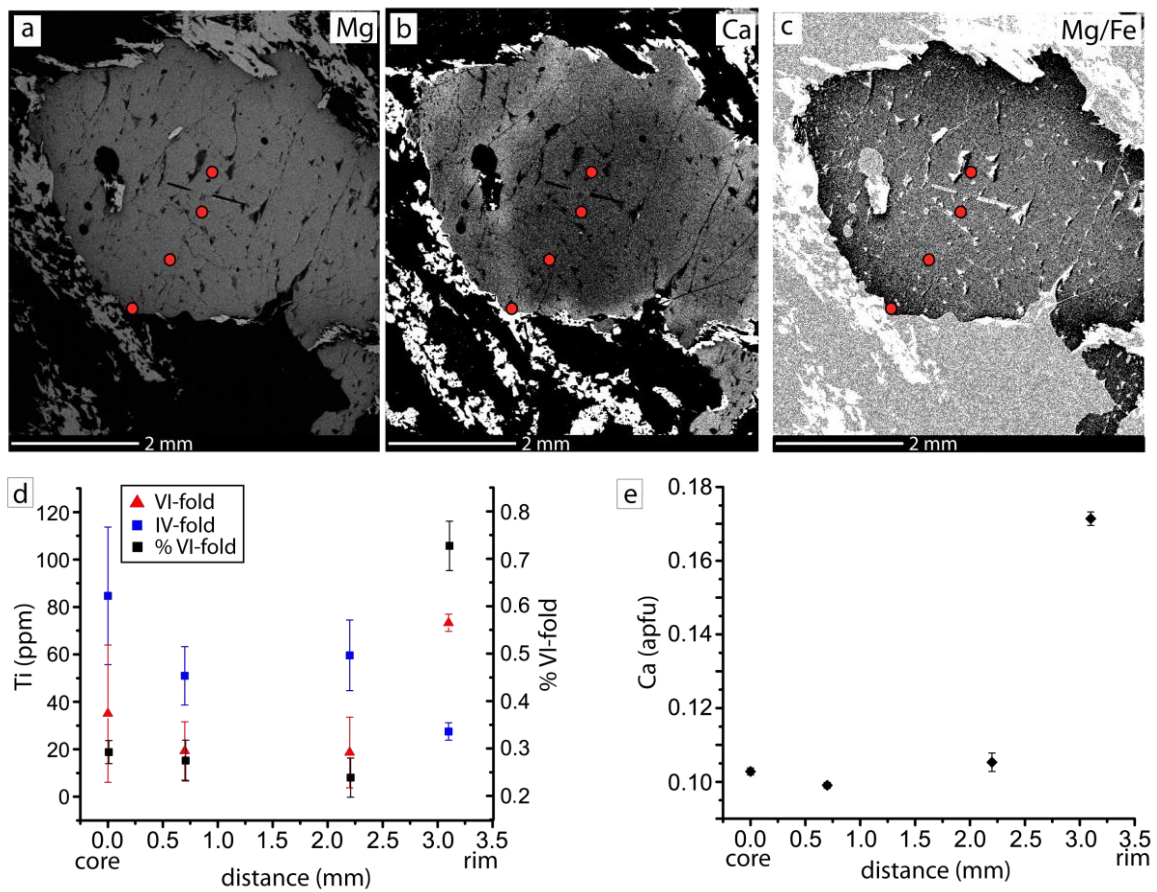
697 **Figure 8**



698

699

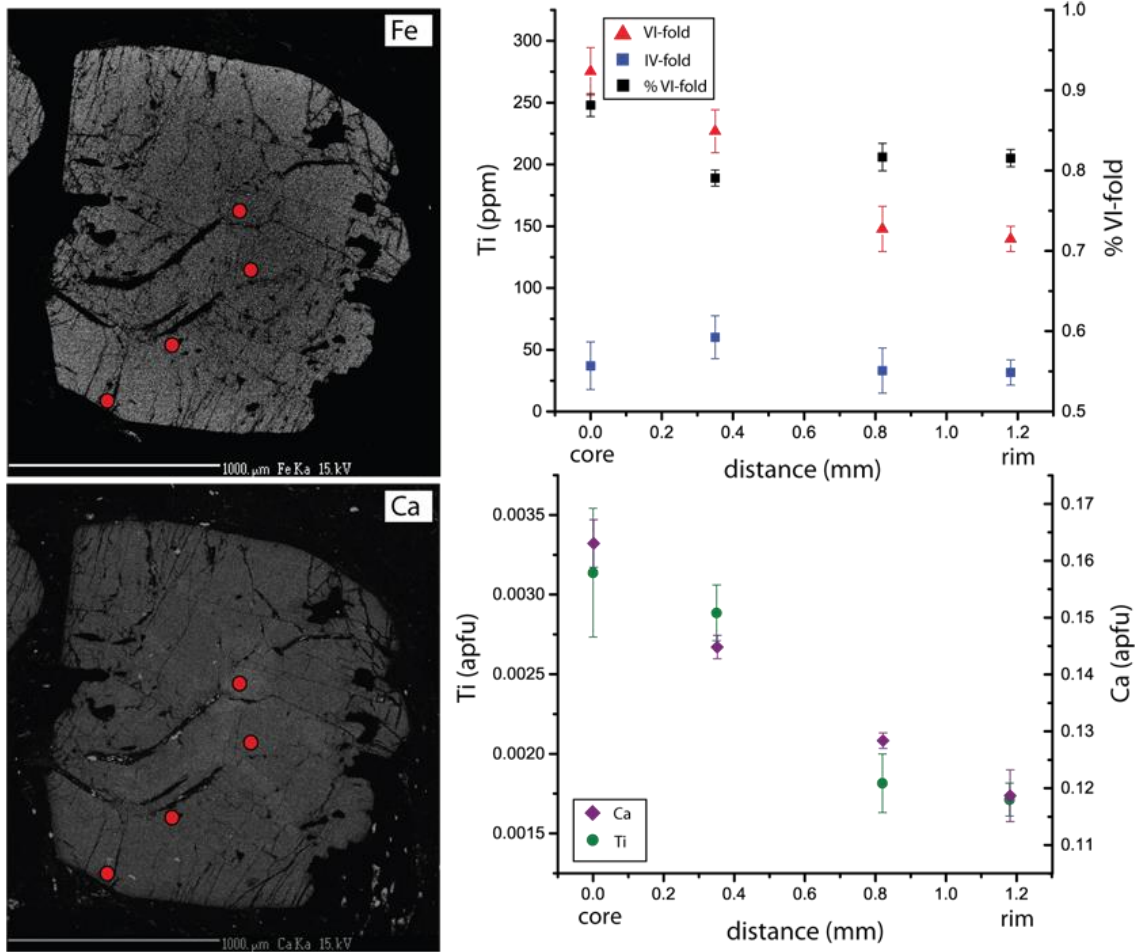
700 **Figure 9**



701

702

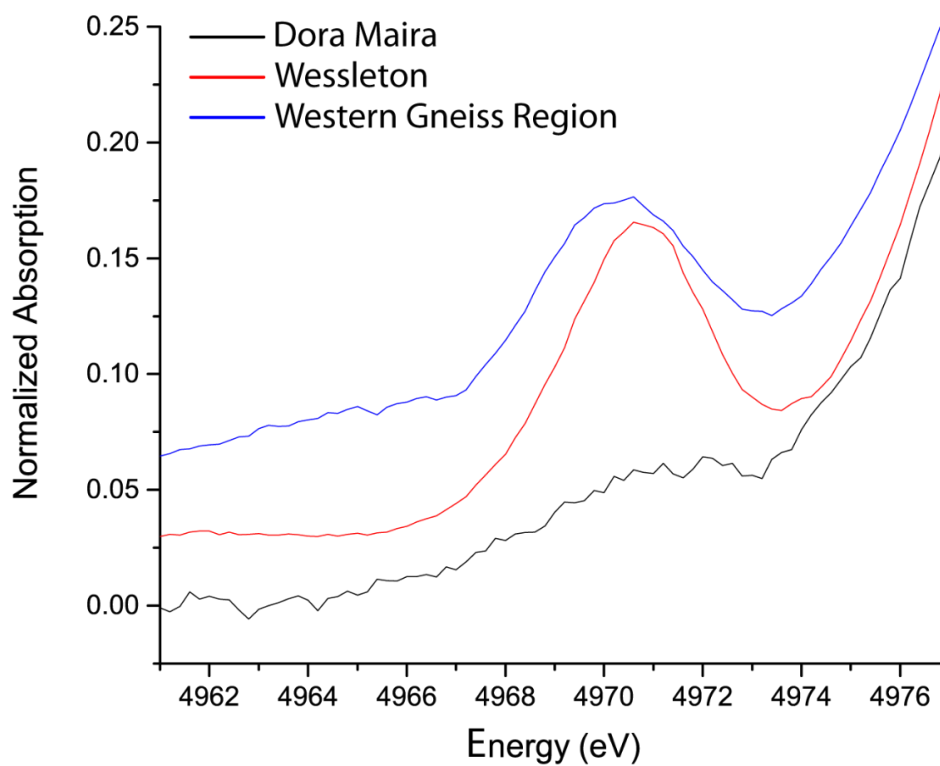
703 **Figure 10**



704

705

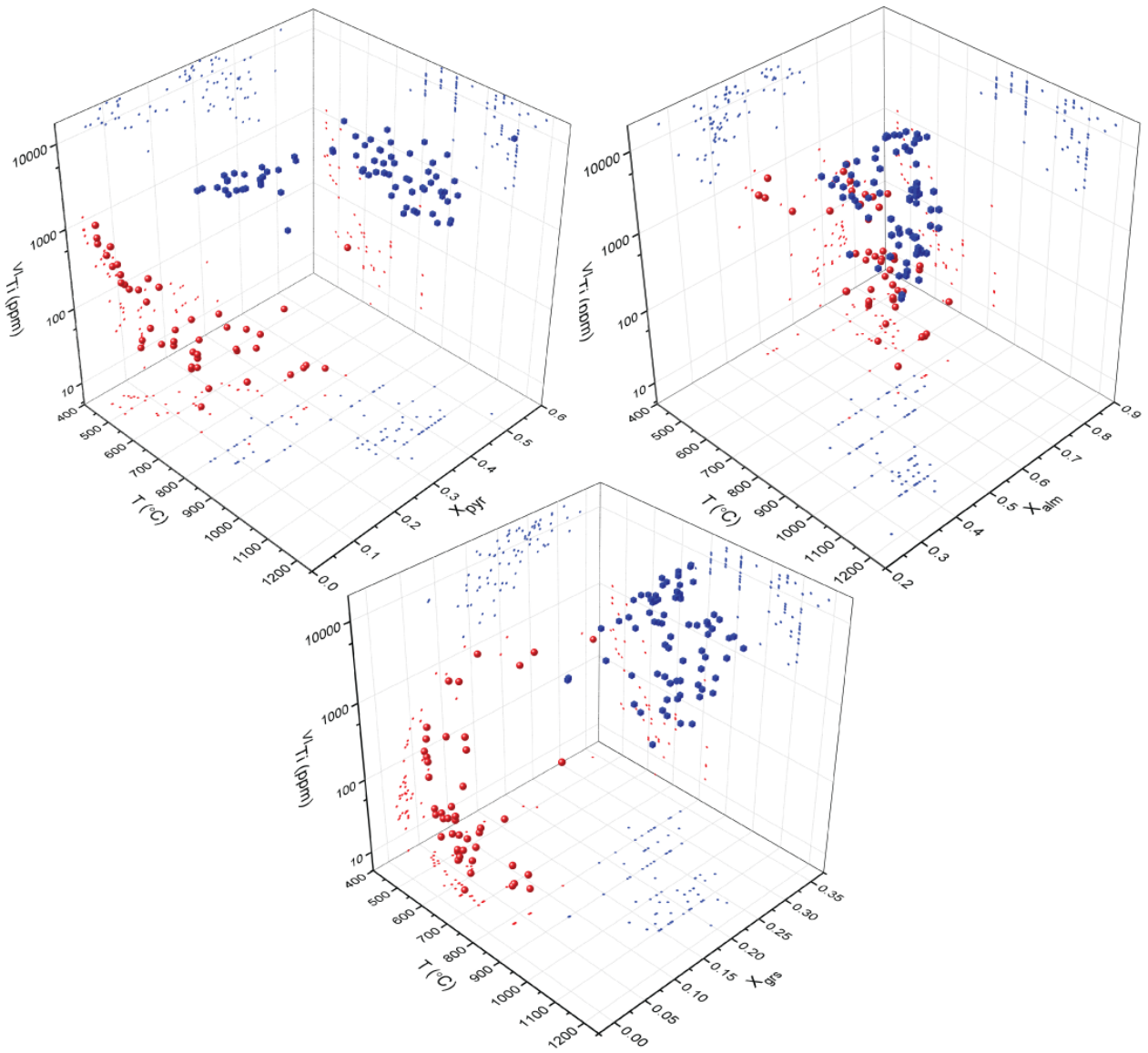
706 **Figure 11**



707

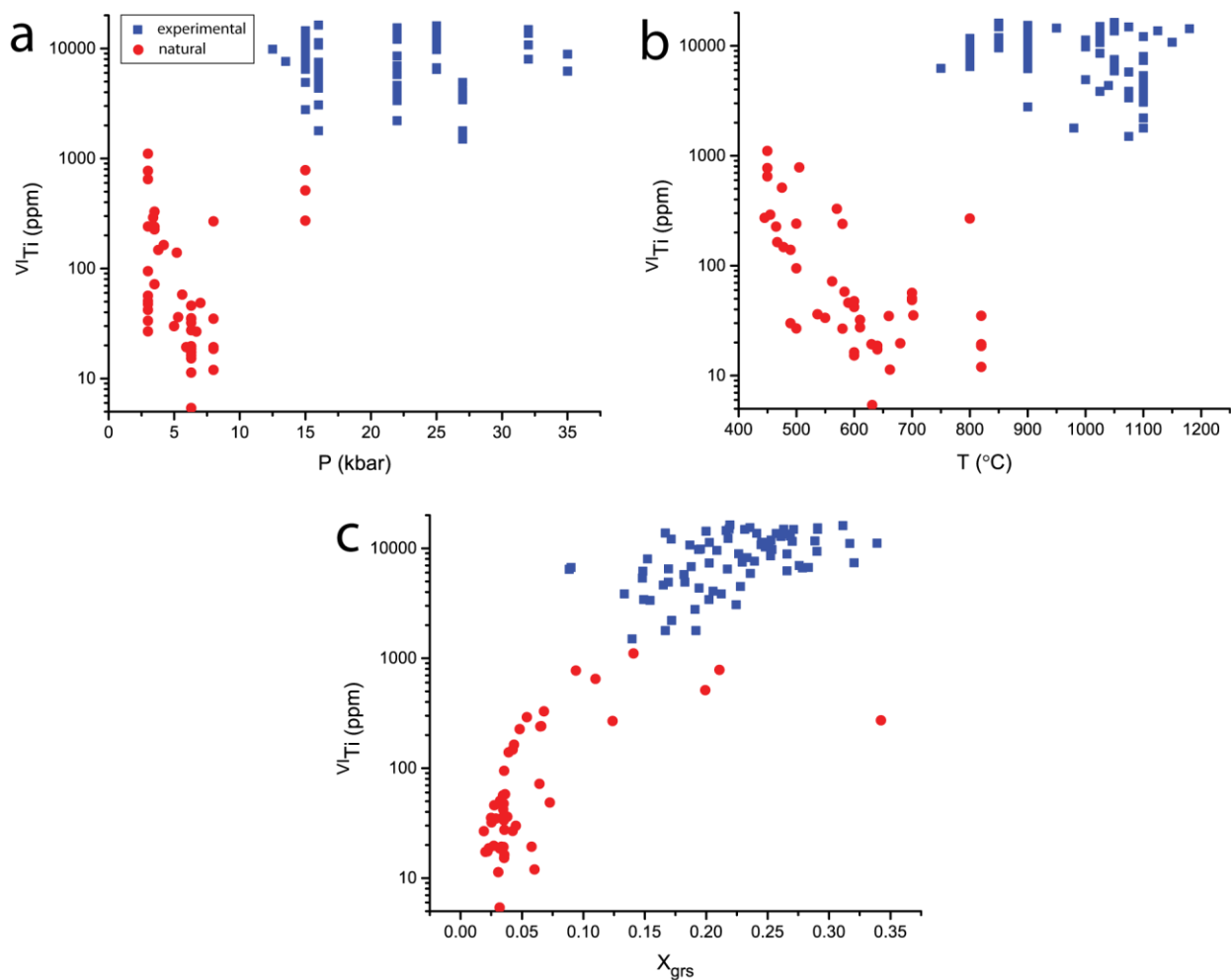
708

709 **Figure 12**



710  
711

712 **Figure 13**



713